We are IntechOpen, the world's leading publisher of Open Access books
Built by scientists, for scientists

6,900
Open access books available

185,000
International authors and editors

200M
Downloads

Our authors are among the

154
Countries delivered to

TOP 1%
most cited scientists

12.2%
Contributors from top 500 universities

WEB OF SCIENCE™

Selection of our books indexed in the Book Citation Index in Web of Science™ Core Collection (BKCI)

Interested in publishing with us?
Contact book.department@intechopen.com

Numbers displayed above are based on latest data collected.
For more information visit www.intechopen.com

7

Thermal Perturbations in Supersonic Transition

Hong Yan
Northwestern Polytechnical University
P.R.China

1. Introduction

In recent years, there has been considerable interest in the study of bump-based methods to modulate the stability of boundary layers (Breuer & Haritonidis, 1990; Breuer & Landahl, 1990; Fischer & Choudhari, 2004; Gaster et al., 1994; Joslin & Grosch, 1995; Rizzetta & Visbal, 2006; Tumin & Reshotko, 2005; White et al., 2005; Worner et al., 2003). These studies are mostly focused on the incompressible regime and have revealed several interesting aspects of bump modulated flows. Surface roughness can influence the location of laminar-turbulent transition by two potential mechanisms. First, they can convert external large-scale disturbances into small-scale boundary layer perturbations, and become possible sources of receptivity. Second, they may generate new disturbances to stabilize or destabilize the boundary layer. Breuer and Haritonidis (Breuer & Haritonidis, 1990) and Breuer and Landahl (Breuer & Landahl, 1990) performed numerical and experimental simulations to study the transient growth of localized weak and strong disturbances in a laminar boundary layer. They demonstrated that the three-dimensionality in the evolution of localized disturbances may be seen at any stage of the transition process and is not necessarily confined to the nonlinear regime of the flow development. For weak disturbances, the initial evolution of the disturbances resulted in the rapid formation of an inclined shear layer, which was in good agreement with inviscid calculations. For strong disturbances, however, transient growth gives rise to distinct nonlinear effects, and it was found that resulting perturbation depends primarily on the initial distribution of vertical velocity. Gaster *et al.*(Gaster et al., 1994) reported measurements on the velocity field created by a shallow oscillating bump in a boundary layer. They found that the disturbance was entirely confined to the boundary layer, and the spanwise profile of the disturbance field near the bump differed dramatically from that far downstream. Joslin and Grosch (Joslin & Grosch, 1995) performed a Direct Numerical Simulation (DNS) to duplicate the experimental results by Gaster *et al.* (Gaster et al., 1994). Far downstream, the bump generated a pair of counter-rotating streamwise vortices just above the wall and on either side of the bump location, which significantly affected the near-wall flow structures. Worner *et al.* (Worner et al., 2003) numerically studied the effect of a localized hump on Tollmien-Schlichting waves traveling across it in a two-dimensional laminar boundary layer. They observed that the destabilization by a localized hump was much stronger when its height was increased as opposed to its width. Further, a rounded shape was less destabilizing than a rectangular shape.

Researchers have also studied the effect of surface roughness on transient growth. White *et al.*(White et al., 2005) described experiments to explore the receptivity of transient disturbances to surface roughness. The initial disturbances were generated by a spanwise-periodic array of roughness elements. The results indicated that the streamwise

flow was decelerated near the protuberances, but that farther downstream the streamwise flow included both accelerated and decelerated regions. Some of the disturbances produced by the spanwise roughness array underwent a period of transient growth. Fischer and Choudhari (Fischer & Choudhari, 2004) presented a numerical study to examine the roughness-induced transient growth in a laminar boundary layer. The results showed that the ratio of roughness size relative to array spacing was a primary control variable in roughness-induced transient growth. Tumin and Reshotko (Tumin & Reshotko, 2005) solved the receptivity of boundary layer flow to a three dimensional hump with the help of an expansion of the linearized solution of the Navier-Stokes equations into the biorthogonal eigenfunction system. They observed that two counter-rotating streamwise vortices behind the hump entrained the high-speed fluid towards the surface boundary layer. Rizzetta and Visbal (Rizzetta & Visbal, 2006) used DNS to study the effect of an array of spanwise periodic cylindrical roughness elements on flow instability. A pair of co-rotating horseshoe vortices was observed, which did not influence the transition process, while the breakdown of an unstable shear layer formed above the element surface played a strong role in the initiation of transition.

Although the effect of physical bumps on flow instabilities has been studied extensively, far fewer studies have explored the impact of thermal bumps. A thermal bump may be particularly effective at supersonic and hypersonic speeds. One approach to introduce the bump is through an electromagnetic discharge in which motion is induced by collisional momentum transfer from charged to neutral particles through the action of a Lorentz force (Adelgren et al., 2005; Enloe et al., 2004; Leonov et al., 2001; Roth et al., 2000; Shang, 2002; Shang et al., 2005). Another approach is through a high-frequency electric discharge (Samimy et al., 2007). Joule heating is a natural outcome of such interactions, and is assumed to be the primary influence of the notional electric discharge plasma employed here to influence flow stability.

For supersonic and hypersonic flows, heat injection for control have considered numerous mechanisms, including DC discharges (Shang et al., 2005), microwave discharges (Leonov et al., 2001) and lasers (Adelgren et al., 2005). Recently however, Samimy *et al.* (Samimy et al., 2007) have employed Localized Arc Filament Plasma Actuators in a fundamentally unsteady manner to influence flow stability. The technique consists of an arc filament initiated between electrodes embedded on the surface to generate rapid (on the time scale of a few microseconds) local heating. Samimy *et al.* (Samimy et al., 2007) employed this method in the control of high speed and high Reynolds number jets. The results showed that forcing the jet with $m = \pm 1$ mode at the preferred column mode frequency provided the maximum mixing enhancement, while significantly reducing the jet potential core length and increasing the jet centerline velocity decay rate beyond the end of the potential core.

Yan *et al.* (Yan et al., 2007; 2008) studied the steady heating effect on a Mach 1.5 laminar boundary layer. Far downstream of the heating, a series of counter-rotating streamwise vortex pairs were observed above the wall on the each side of the heating element. This implies that the main mechanism of the thermal bump displays some degree of similarity to that of the physical bump. This finding motivates the further study on thermal bumps since they have several advantages over physical bumps. These include the ability to switch on and off on-demand, and to pulse at any desired frequency combination. Yan and Gaitonde (Yan & Gaitonde, 2010) studied both the steady and pulsed thermal rectangular bumps in supersonic boundary layer. For the steady bump, the velocity fluctuation profile across the span bore some similarity to the physical bump in an overall sense. The disturbance decayed

downstream, suggesting that the linear stability theory applies. For pulsed heating, non-linear dynamic vortex interactions caused disturbances to grow dramatically downstream. Yan and Gaitonde (Yan & Gaitonde, 2011) assessed the effect of the geometry of the thermal bump and the pulsing properties. It was shown that the rectangular element was more effective than the circular counterpart. The smaller width of the rectangular element produced higher disturbance energy, while the full-span heating indicated delayed growth of the disturbances. The disturbance energy increased with the initial temperature variation, and the lower frequency produced lesser disturbance energy.

This chapter summarizes some of the key findings in thermal perturbation induced supersonic flow transition in our research group. The chapter is organized as follows. The flow configuration, setup and numerical components are described first. The effect of the pulsed heating is then explored in the context of disturbance energy growth, and correlated with linear stability analysis. Subsequently, the phenomenology of the non-linear dynamics between the vortices produced by the pulsed bump and the compressible boundary layer is examined with emphasis on later stages of the boundary layer transition.

2. Flow configuration

A Mach 1.5 flat plate flow is considered with the total temperature and pressure of 325 K and 3.7×10^5 Pa, respectively. The thermal bump is imposed as a surface heating element and centered in the spanwise direction as shown schematically in Fig. 1. For some simulations, the

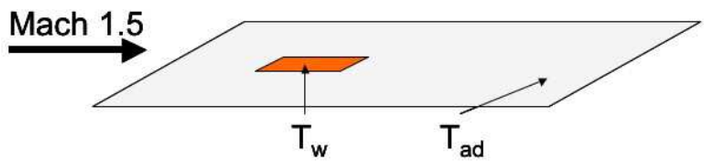

Fig. 1. Flat plate with thermal bump

nominally two-dimensional case is considered where the bump extends cross the entire span of the plate. Even for this case, the three-dimensional domain is discretized since the primary disturbance growth is three-dimensional. The heating effect is modeled as a time-dependent step surface temperature rise ΔT_w with a monochromatic pulsing frequency (f) and duty cycle as shown in Fig. 2, where the pulsing time period $T_t = 1/f$. The subscript w denotes the value at the wall. For simplicity, it is assumed that $\Delta T_w = T_w - T_{w0}$, where T_w and T_{w0} are wall temperature inside and outside of the heating region, respectively, and T_{w0} is fixed at the adiabatic temperature (T_{ad}) as shown in Fig. 1.

In all perturbed simulations, the heating element is placed immediately upstream of the first neutral point in the stability neutral curve for an adiabatic flat plate boundary layer with the freestream Mach number (M_∞) of 1.5. The stability diagram, shown in Fig. 3, is obtained from the Langley Stability and Transition Analysis Codes (LASTRAC) (Chang, 2004). LASTRAC performs linear calculations and transition correlation by using the N-factor method based on linear stability theory, where the N factor is defined by $N = \int_{s_0}^{s_1} \gamma ds$, and s_0 is the point at which the disturbance first begins to grow, s_1 is the end point of the integration, which may be at upstream or downstream of where transition is correlated and γ is the characteristic growth rate of the disturbance. For disturbances at $f = 100$ kHz, the first neutral point is located at the Reynolds number of $Re = 610$ based on the similarity boundary-layer length scale (η) defined as $= \sqrt{\nu_\infty x/u_\infty}$, where ν_∞ and u_∞ are the freestream kinematic viscosity

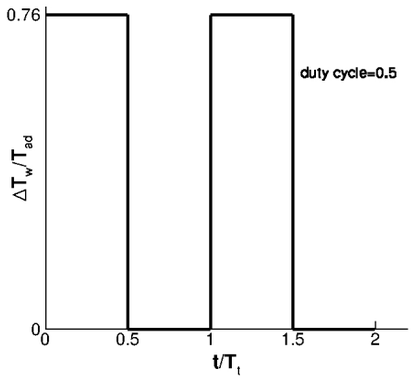

Fig. 2. Two time periods of surface temperature rise, T_t

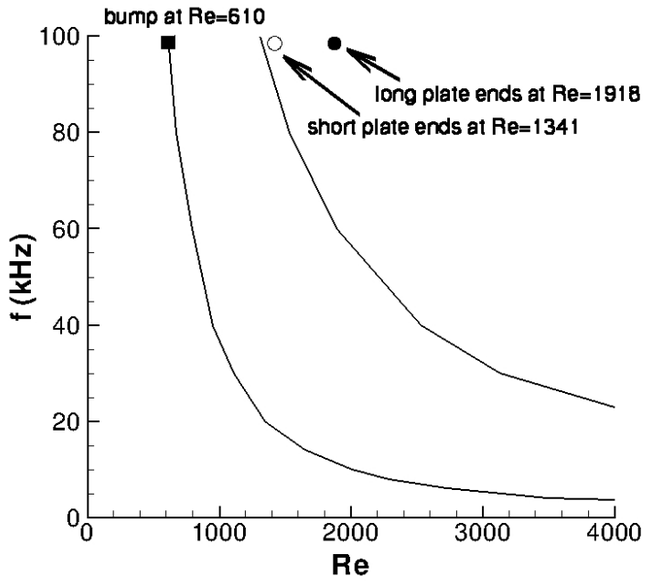

Fig. 3. Neutral curve for Mach 1.5 adiabatic flat plate boundary layer

and streamwise velocity, respectively and is shown as the solid rectangle in Fig. 3. The local Reynolds number based on the running distance from the leading edge of the plate[1] is defined by $Re_x = Re^2$. Thus, the distance from the leading edge of the plate to the leading edge of the heating element is 7.65 mm (*i.e.* corresponding to $Re = 610$). The nominal spanwise distance between bumps is determined from the most unstable mode, which for the present Mach number is oblique. The N factor profile, shown in Fig. 4 for different spanwise wave lengths (λ) at M_∞=1.5 and $f = 100$ kHz, indicates that $\lambda = 2$ mm is the most unstable mode. Thus, the nominal distance between two adjacent heating elements is set to 2 mm to excite the most unstable wave. This is accomplished by choosing a spanwise periodic condition on a domain of 2 mm, at the center of which a bump is enforced.

[1] Re_x grows linearly with x and is adopted in all the figures and tables except in the neutral stability curve figure, where Re is used instead.

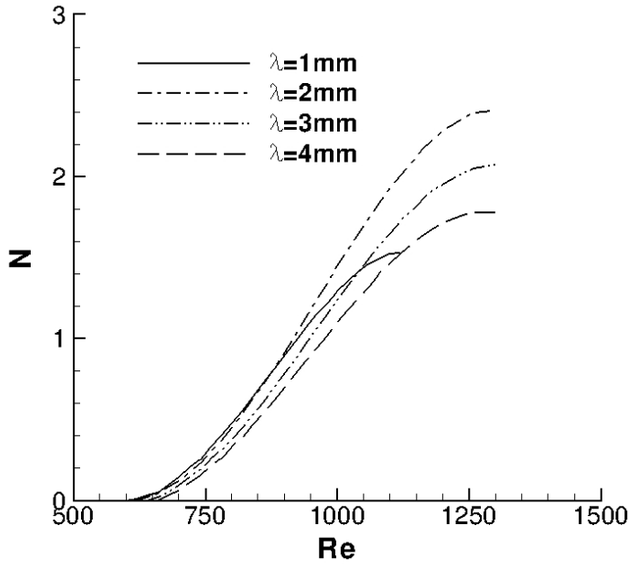

Fig. 4. N factor for different spanwise wavelengths at Mach=1.5 and $f = 100$ kHz

3. Numerical model

The governing equations are the full compressible 3-D Navier-Stokes equations. The Roe scheme (Roe, 1981) is employed together with the Monotone Upstream-centered Schemes for Conservation Laws (MUSCL)(Van Leer, 1979) to obtain up to nominal third order accuracy in space. Solution monotonicity is imposed with the harmonic limiter described by Van Leer (Van Leer, 1979). Given the stringent time-step-size limitation of explicit schemes, an implicit approximately factored second-order time integration method with a sub-iteration strategy is implemented to reduce computing cost. The time step is fixed at 4.2×10^{-8} s for all the cases.

The Cartesian coordinate system is adopted with x, y and z in the streamwise, wall-normal and spanwise direction, respectively. The x axis is placed through the center of the plate with the origin placed at the leading edge of the plate. The computational domain is L_x =38 mm long, L_y =20 mm high and L_z =2 mm wide for case 1, and L_x =76 mm long, L_y =51 mm high and Lz =2 mm wide for cases 2 and 3. This is determined by taking two factors into consideration. In the streamwise direction, the domain is long enough to capture three-dimensional effects induced by heating and to eliminate the non-physical effects at the outflow boundary. Based on this constraint, the Reynolds number at the trailing edge of the plate is $Re_L = 1.80 \times 10^6$ for case 1, and 3.68×10^6 for cases 2 and 3. In the wall-normal direction, the domain is high enough to avoid the reflection of leading edge shock onto the surface. The upper boundary is positioned at $86\delta_L$ above the wall for case 1, and $220\delta_L$ for cases 2 and 3, where δ_L is the boundary layer thickness at the trailing edge of the plate. The velocity, pressure and density in the figures shown in Section *Results and analyses* are normalized by u_∞, p_∞ and ρ_∞, respectively. The vorticity is normalized by u_∞ / L_x, where $u_\infty = 450$ m/s and L_x =0.038 m.

The grid is refined near the leading edge of the flat plate and near the heating element. Approximately 150 grid points are employed inside the boundary layer at the leading edge of

the heating element to resolve the viscous layer and capture the heat release process. Previous results (Yan & Gaitonde, 2008) indicated that this is fine enough to capture the near-field effect of the thermal perturbation. The grid sizes are $477 \times 277 \times 81$ in the x, y and z direction, respectively for case 1, and $854 \times 297 \times 81$ for cases 2 and 3.

For boundary conditions, the stagnation temperature and pressure and Mach number are fixed at the inflow. The no-slip condition with a fixed wall temperature is used on the wall. The pulse is imposed as a sudden jump as shown in Fig. 2. The symmetry condition is enforced at the spanwise boundary to simulate spanwise periodic series of heating elements spaced L_z apart in the finite-span bump cases. This boundary condition is also suitable to mimic two-dimensional perturbation in the full-span bump case. First-order extrapolation is applied at the outflow and upper boundaries.

4. Results and analyses

The study is comprised of two parts. The first part studies the effects of the pulsed bump whose properties are listed in case 1 in Table 1. The pulsed bump introduces the disturbance at $f = 100$ kHz, and is located at $Re_0 = 610^2 = 0.3721 \times 10^6$, immediately upstream of the first neutral point (Re=610) for this particular frequency, where the subscript 0 denotes the streamwise location of the thermal bump. The Reynolds number at the trailing edge of the plate is $Re_L = 1341^2 = 1.80 \times 10^6$, which corresponds to the location immediately downstream of the second neutral point (Re =1300) as shown in Fig. 3. The rectangular bump is considered with spanwise width (w) of 1 mm and its streamwise length (l) is arbitrarily set to 0.2 mm.

Case	w/l (mm)	f (kHz)	$Re_L \times 10^{-6}$
1	1/0.2	100	1.80
2	1/0.2	100	3.68
3	2/0.2 (full span)	100	3.68

Table 1. Classification of cases simulated, $\Delta T_w = 0.76 T_{ad}$, $Re_0 = 0.3721 \times 10^6$

The second part examines the breakdown process at later stages of flow evolvement. To this end, the plate is extended far downstream of the second neutral point to $Re = 1918$ ($Re_L = 3.68 \times 10^6$) as shown in Fig. 3. Both 3D and 2D thermal bumps are considered. The cases are denoted as cases 2 and 3 in Table 1.

4.1 Effect of pulsed bump

4.1.1 Unperturbed flow (basic state)

The basic or unperturbed state is a Mach 1.5 adiabatic flat plate boundary layer with Reynolds number at the trailing edge of the plate of $Re_L = 1.80 \times 10^6$. Figs. 5 and 6 show the streamwise and wall-normal velocity profiles along the y direction at $Re_x = 1.4 \times 10^6$ at the spanwise center and side of the plate. The y coordinate is normalized with the local theoretical boundary layer thickness (δ). Both boundary layer thickness and velocity profiles are predicted correctly compared to the compressible boundary layer theory. In particular, the wall-normal velocity, which is of much smaller order $v \sim u_\infty / \sqrt{Re_x}$, is captured correctly as well. The fact that the profiles on the center and side of the plate collapse demonstrates flow two-dimensionality as expected.

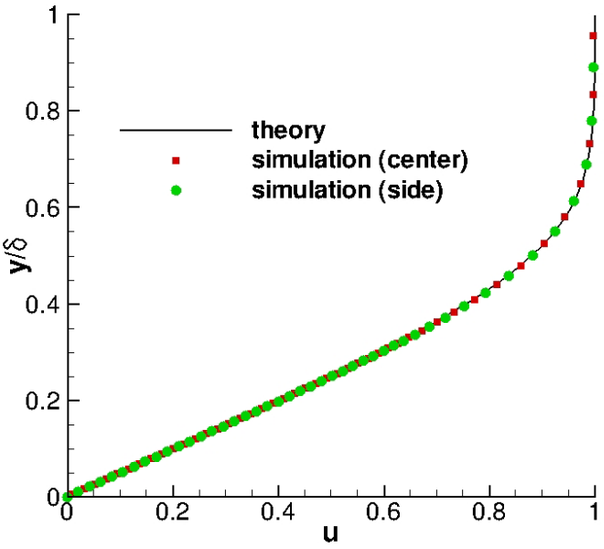

Fig. 5. Streamwise velocity in the y direction at $Re_x = 1.4 \times 10^6$ (basic state for case 1)

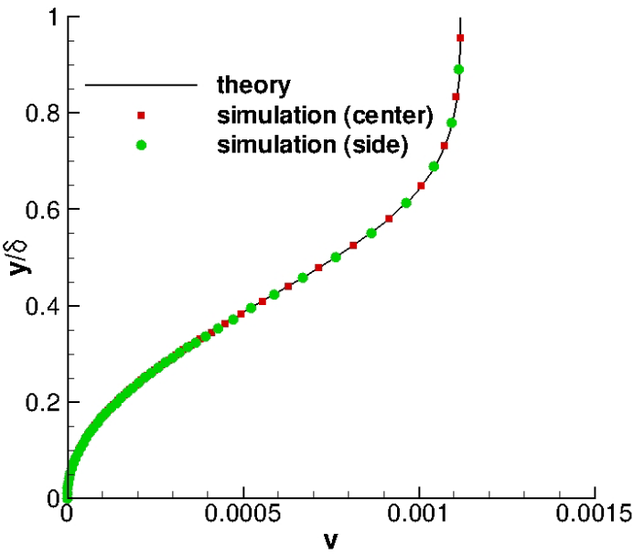

Fig. 6. Vertical velocity in the y direction at $Re_x = 1.4 \times 10^6$ (basic state for case 1)

4.1.2 Perturbed flow by pulsed bump

A pulsed thermal bump at a frequency of 100 kHz is turned on to introduce the disturbance after the basic state is obtained. Recall that the bump is placed immediately upstream of the first neutral point (where $Re = 610$) for disturbances at frequency of 100 kHz.

For all the pulsed heating cases, the solution is marched until a statistically stationary state is obtained. This determination is made by monitoring all primitive variables at several points in the domain. Mean statistics are then gathered over numerous cycles until time invariant values are obtained. The instantaneous results presented are those obtained after the time-mean quantities reach invariant values.

Fig. 7 shows the instantaneous streamwise vorticity contours on the wall. Since these values

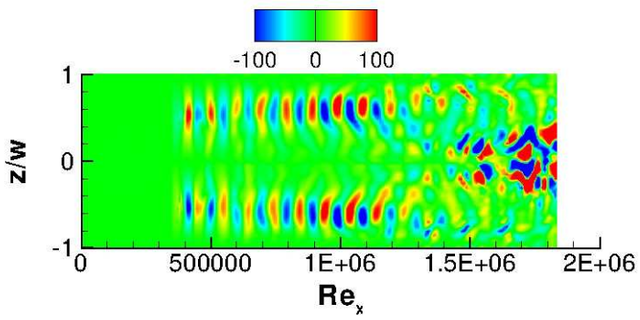

Fig. 7. Instantaneous ω_x contours on the wall (case 1)

are plotted after the flow reaches an asymptotic state, the vortex pattern is formed by the dynamic vortex interaction from numerous heating pulses. When the bump is pulsed, a complex vortex shedding and dynamic interaction process results in a vortical pattern with the alternating sign in the streamwise direction. These structures are constrained in the spanwise direction, but move away from the surface, which will be shown in the time-mean values. Smaller eddies are observed at about $Re_x = 1.25 \times 10^6$ near the central region and intensified downstream of $Re_x = 1.5 \times 10^6$.

The effect of pulsing on the time-mean streamwise vorticity is shown in Fig. 8. The spanwise-varying streaky structures are formed downstream with concentration in the central

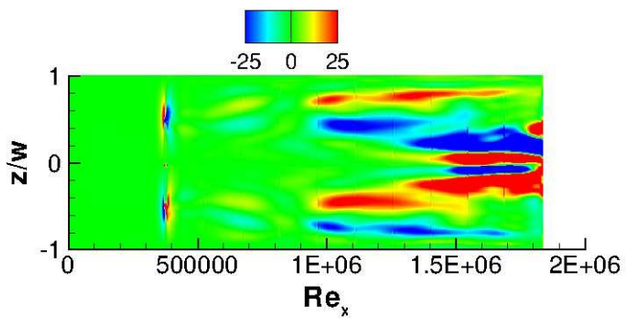

Fig. 8. Time-mean ω_x contours on the wall (case 1)

region and intensified after $Re_x = 1.5 \times 10^6$. These results bear some similarity to free shear flow control with tabs. For example, Zaman *et al.* (Zaman et al., 1994) demonstrated with a comprehensive experimental study that the pressure variation induced by the tabs installed on the nozzle wall generated streamwise vorticity, which significantly enhanced the mixing downstream of the nozzle exit.

The vortex interaction and penetration can be seen on the cross sections in Fig. 9. The first cross section (Fig. 9(a)) is cut immediately downstream of the bump, therefore the top pair

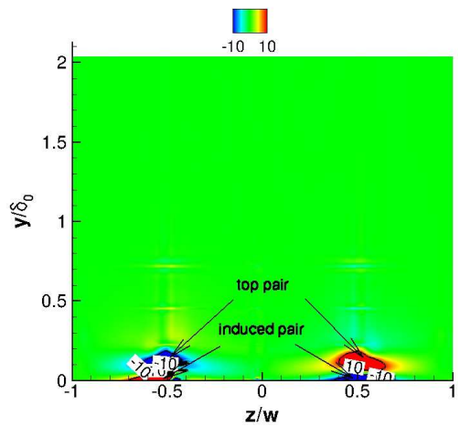

(a) $Re_x = 0.38 \times 10^6$

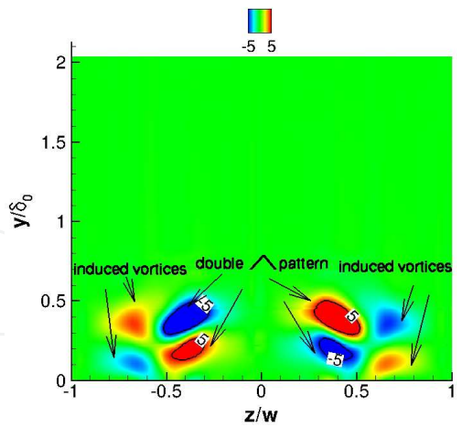

(b) $Re_x = 0.5 \times 10^6$

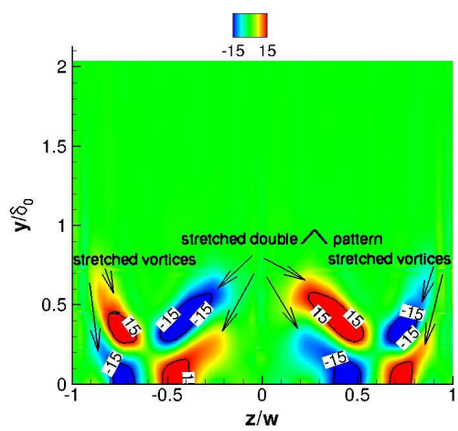

(c) $Re_x = 1.0 \times 10^6$

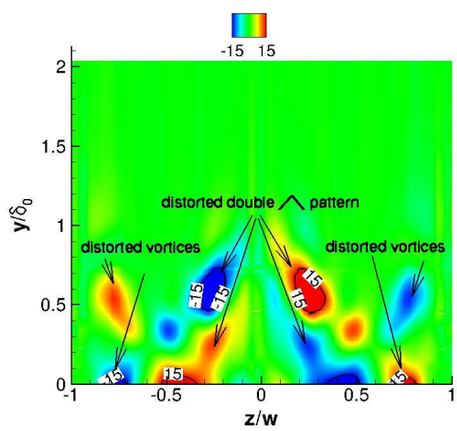

(d) $Re_x = 1.25 \times 10^6$

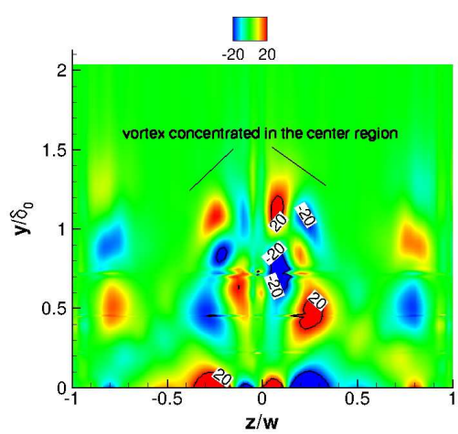

(e) $Re_x = 1.5 \times 10^6$

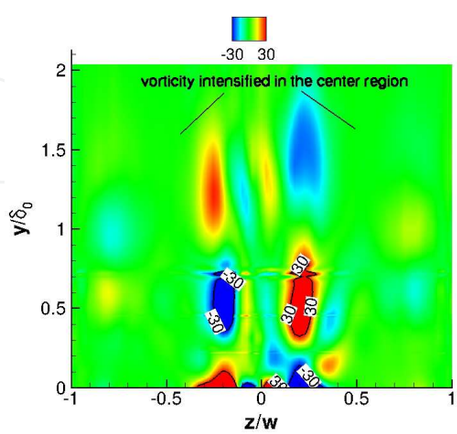

(f) $Re_x = 1.75 \times 10^6$

Fig. 9. Time-mean ω_x on different cross sections (case 1)

of vortices above the wall possesses the same sign as that at the leading edge of the bump shown in Fig. 8 (positive at $z = 0.5w$ and negative at $z = -0.5w$). As they move downstream, they are lifted away from the wall and induce additional vortices near the wall to satisfy the noslip condition as well on the sides where periodic conditions apply. The original pairs form a double $\bigwedge$ pattern as indicated in Fig. 9(b). As they move downstream, vortices are stretched and intensified as shown in Fig. 9(c). At $Re_x = 1.25 \times 10^6$ (Fig. 9(d)), the vortex pattern is distorted and the vortices break into smaller eddies. This leads to the complex vortex dynamic interaction downstream at $Re_x = 1.5 \times 10^6$ (Fig. 9(e)), which completely distorts the double $\bigwedge$ pattern and results in a vortex trace that appears to move towards the center region. At the last station (Fig. 9(f)), the vorticity is intensified around the center region.

The accumulated effect of the streamwise vorticity distorts the basic state in nonlinear fashion. Fig. 10 shows the streamwise perturbation velocity contours on the downstream cross sections. The quantity plotted is $\bar{u} - u_b$, where $\bar{u}$ is the time-mean value of the pulsed case. Please note change in contour levels between Figs. 9 and 10. Immediately downstream of the bump (Fig. 10(a)), a velocity excess region is formed above the wall due to flow expansion. Proceeding downstream, a velocity deficit is generated downstream of the center of the heating element, while an excess is observed on both sides of the bump (Fig. 10(b)). This behavior is similar to the observation in the flow over a shallow bump studied by Joslin and Grosch (Joslin & Grosch, 1995) and the steady heating case discussed earlier. The intensity of the excess region is at the same level as that in the steady heating (compare Fig. 10(a) with Fig. 9(a)). Proceeding downstream, the pulsed bump behaves differently from the steady one. The velocity distortion is amplified as seen in Figs. 10(c) and (d). The velocity excess regions grow in the region near the wall across the entire span of the domain (Figs. 10(e) and (f)) as the streamwise vortices bring the high-momentum fluid from the freestream towards the wall.

The above observations are further explored in Fig. 11, which plots $\bar{u}$ and $u' = \bar{u} - u_b$ along the y direction at z=0 and z=-0.5w (*i.e.*, at the spanwise edge of the bump). The intensity of the velocity excess in the near-wall region increases along the downstream and reaches about 20% of u_∞ at $Re_x = 1.75 \times 10^6$, while in the outer region, a velocity deficit is observed. This results in an inflection point in the mean flow near the centerline (Fig. 11(a)), giving rise to the rapid breakdown observed in Fig. 9. On the edges of the bump, the flow is accelerated cross the entire boundary layer and no inflection points are observed (Fig. 11(b)).

The strength of disturbance energy growth for the compressible flow is measured by the energy norm proposed by Tumin and Reshotko (Tumin & Reshotko, 2001) as

$$E = \int_0^\infty \vec{q}^T A \vec{q} dy \tag{1}$$

where $\vec{q}$ and A are the perturbation amplitude vector and diagonal matrix, respectively, and are expressed as

$$\vec{q} = (u', v', w', \rho', T')^T \tag{2}$$

$$A = diag[\rho, \rho, \rho, T/(\gamma \rho M_\infty^2), \rho/(\gamma(\gamma - 1)TM_\infty^2)] \tag{3}$$

The first three terms represent the components of the kinetic disturbance energy denoted as E_u, E_v and E_w, respectively and the last two represent the thermodynamic disturbance energy as E_ρ and E_T. The spanwise-averaged disturbance energy is plotted in Fig. 12. The initial growth rate of the total disturbance energy is small and becomes larger as the disturbances are amplified in the region of $0.9 \times 10^6 < Re_x < 1.4 \times 10^6$. The disturbances then saturate and reach finite amplitude shown as a plateau in Fig. 12(a). At this stage, the flow reaches

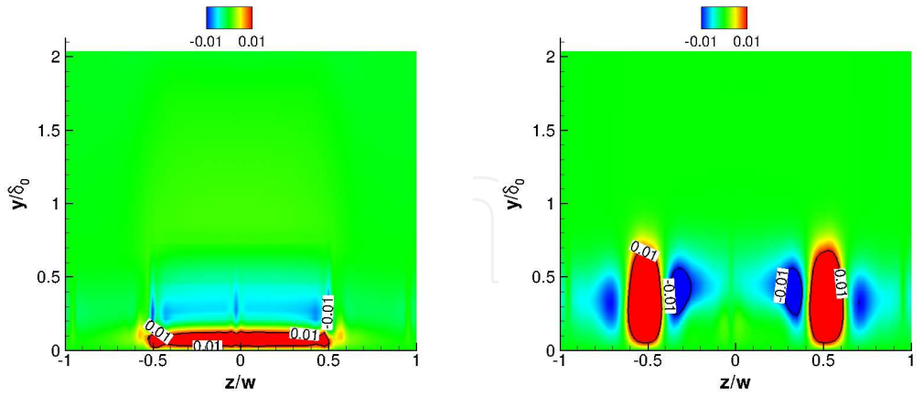

(a) $Re_x = 0.38 \times 10^6$

(b) $Re_x = 0.5 \times 10^6$

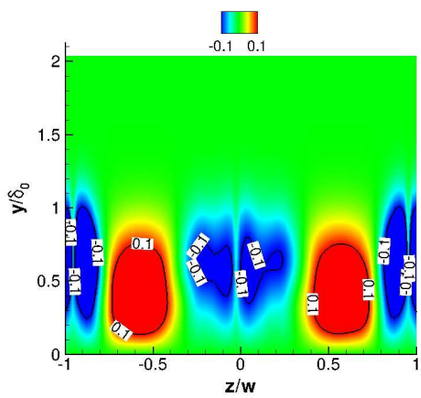

(c) $Re_x = 1.0 \times 10^6$

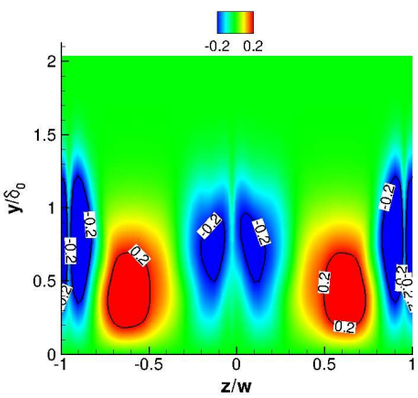

(d) $Re_x = 1.25 \times 10^6$

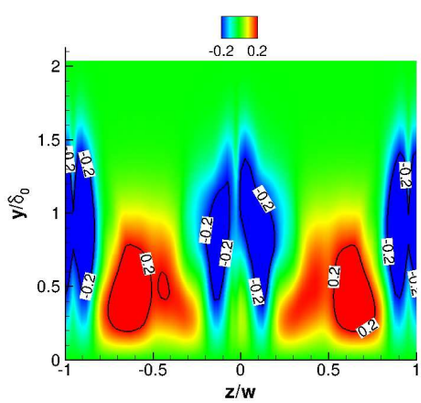

(e) $Re_x = 1.5 \times 10^6$

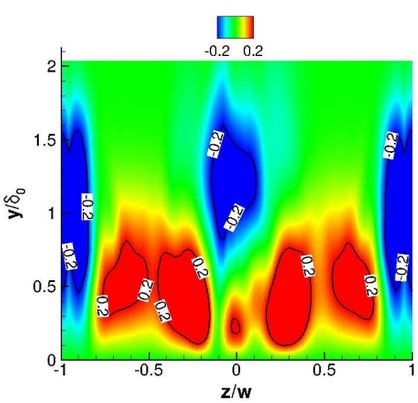

(f) $Re_x = 1.75 \times 10^6$

Fig. 10. $u' = \bar{u} - u_b$ on different cross sections (case 1)

a new state which becomes a basic state on which secondary instabilities can grow (Schmid & Henningson, 2001). The new basic state is represented by the appearance of the inflection point at $Re_x = 1.5 \times 10^6$ in the left plot of Fig. 11(a). The disturbances grow more rapidly after $Re_x = 1.5 \times 10^6$ because the secondary instability susceptible to high frequency disturbances usually grows more rapidly than the primary instabilities. The thermodynamic disturbance energy (E_ρ and E_T) in Fig. 12 (b) shows a similar trend except for a spike in the vicinity of the thermal bump as expected. However the thermodynamic components are four orders of magnitude lower than the E_u, indicating that the primary disturbance quickly develops a vortical nature.

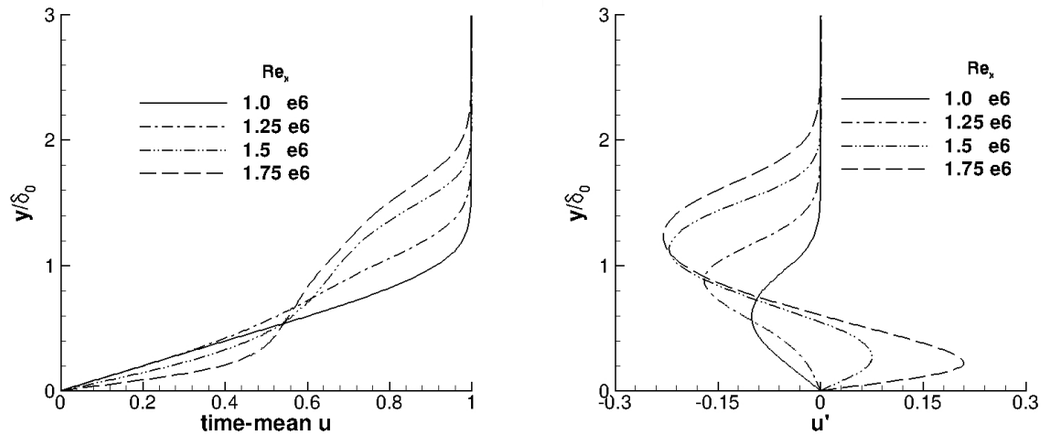

(a) at $z = 0$

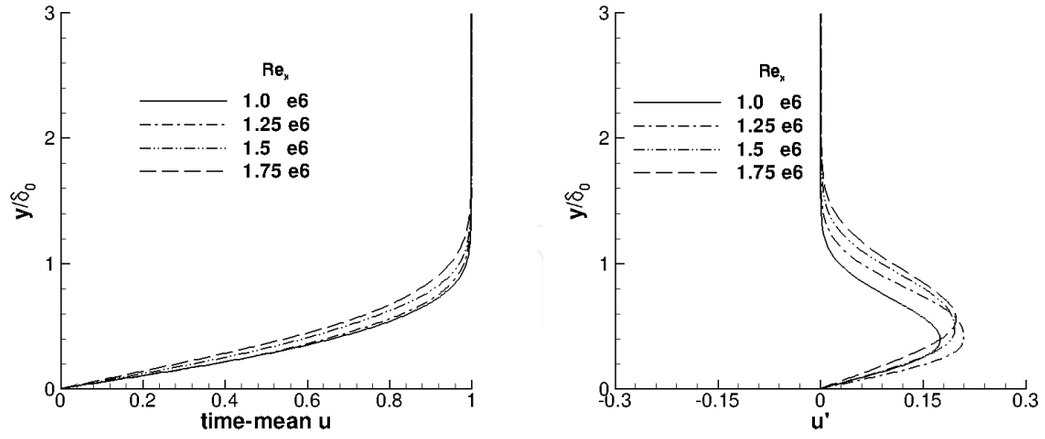

(b) at $z = -0.5w$

Fig. 11. $\bar{u}$ and $u' = \bar{u} - u_b$ along the y direction (case 1)

With pulsed heating, the disturbances grow significantly downstream and the flow becomes highly inflectional. The observation is consistent with the linear stability theory. However the velocity fluctuation reaches 20% of u_∞ at the downstream, indicating that non-linear growth comes into the play and the assumption that disturbances are infinitesimal is not valid any

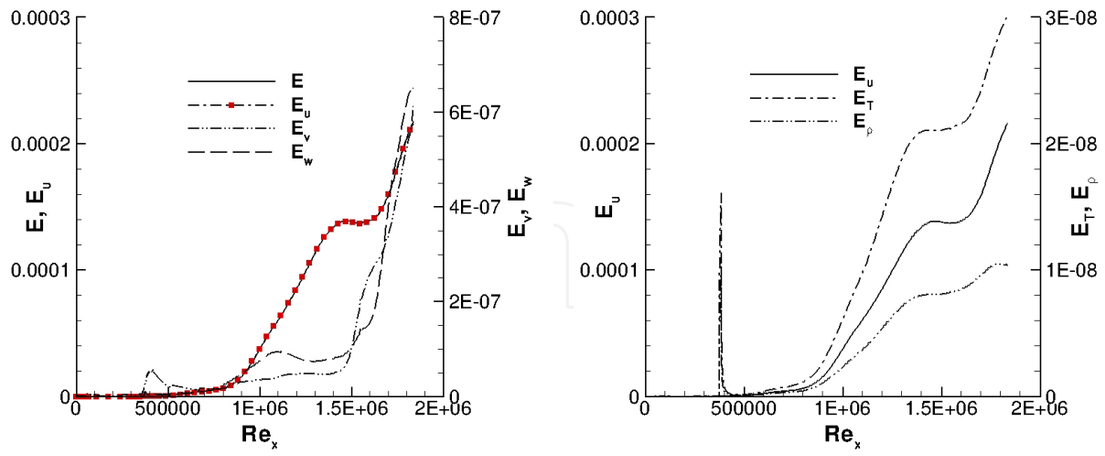

(a) E, E_u, E_v and E_w (b) E_u, E_T and E_ρ

Fig. 12. Spanwise-averaged disturbance energy along the x direction (case 1)

more. Thus, the dynamic vortex non-linear interaction plays an important role in the later development of the sustained disturbance growth, and will be discussed in the following section.

4.2 Analyses of breakdown process

This section explores the phenomenology of the non-linear dynamics between the vortices produced by the bump and the compressible boundary layer. To this end, the domain size is extended in both streamwise and normal directions relative to the case 1, but the spanwise width remains unchanged. The Reynolds number at the end of the plate is $Re_L = 3.68 \times 10^6$. Two cases (cases 2 and 3 in Table 1) are examined; the first considers a three-dimensional perturbation associated with a finite-span thermal bump, and the second is comprised of full-span disturbances. In both cases, the bump is positioned at the same streamwise location as in the case 1 with the same pulsing frequency and magnitude shown in Table 1.

A new basic state (no perturbation) is obtained for the cases with the extended domain. In the absence of imposed perturbations, no tendency is observed towards transition even at the higher Reynolds number. Figs. 13 and 14 show the streamwise and wall-normal velocity profiles along the y direction at $Re_x = 3.5 \times 10^6$. The comparisons with the compressible theoretical profiles are good and the fact that the profiles on the center and side of the plate collapse demonstrates flow two-dimensionality as expected.

The heating element is turned on after the basic state is obtained. For the finite-span case, a series of counter-rotating streamwise vortices are generated at the edges of the thermal bump by heating induced surface pressure variation as discussed earlier. These vortices shed from their origins when the element is switched off, forming a traveling vortical pattern with an alternating sign in the streamwise direction up to $Re_x = 1.25 \times 10^6$ as shown in Fig. 15(a), where the instantaneous streamwise vorticity contours are plotted on the wall. Further downstream, small organized alternating structures appear near the center region at $Re_x = 1.5 \times 10^6$. Up to this point, the perturbed flow structures are similar to case 1 as expected. Subsequently, the vortices are intensified at about $Re_x = 2.0 \times 10^6$ due to vortex stretching

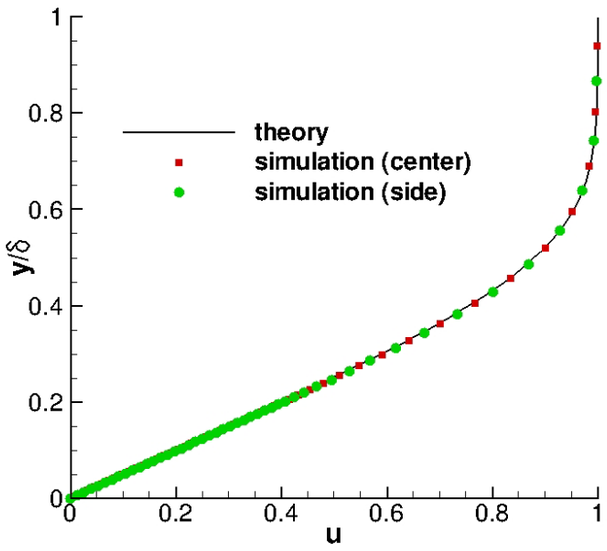

Fig. 13. Streamwise velocity in the y direction at $Re_x = 3.5 \times 10^6$ (basic state for cases 2 and 3)

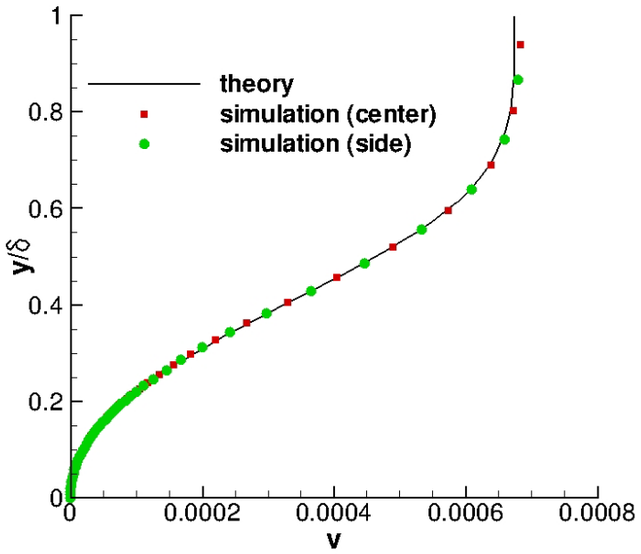

Fig. 14. Vertical velocity in the y direction at $Re_x = 3.5 \times 10^6$ (basic state for cases 2 and 3)

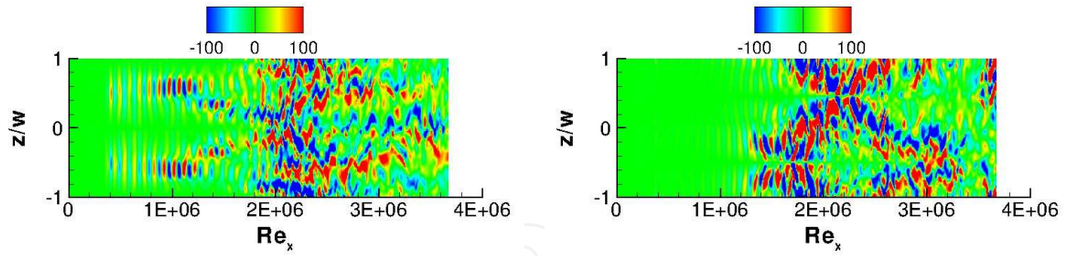

(a) finite span (b) full span

Fig. 15. Instantaneous ω_x contours on the wall (cases 2 and 3)

and interaction, which is described in more detail later. After $Re_x = 2.5 \times 10^6$, the flow tends to relax to a relatively universal stage. The full-span case shows a different development as shown in Fig. 15(b). The counter-rotating vortices are not observed immediately downstream of the bump. Rather, an asymmetric instantaneous vortical pattern is initiated with small successive structures starting at about $Re_x = 1.25 \times 10^6$, which are concentrated on the lower half of the domain. The fact that these small structures occur at the same location for both cases suggests that they are unlikely to be related to the original counter-rotating vortices, and an inherent stability mechanism that stimulates their appearance.

The vortex development is examined in a three-dimensional fashion in Fig. 16 which shows the iso-surface of the non-dimensionalized vorticity magnitude at $|\omega| = 100$ colored with

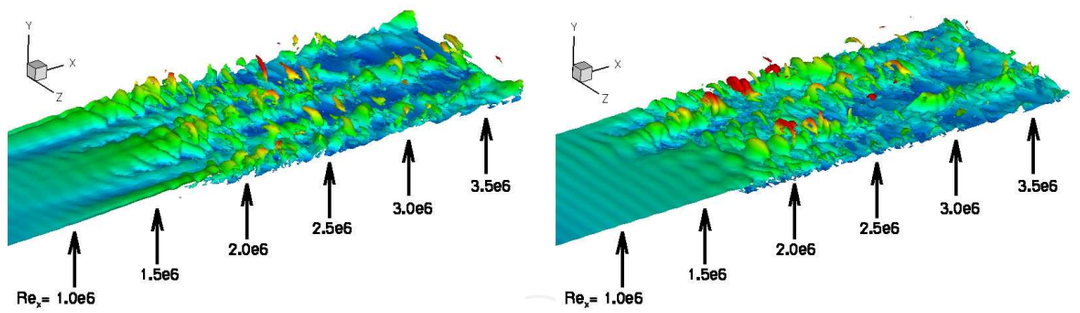

(a) finite span (b) full span

Fig. 16. Iso-surface of instantaneous vorticity magnitude at $|\omega| = 100$, $x : y = 1 : 10$, $x : z = 1 : 10$ (cases 2 and 3)

the distance from the wall. This iso-level is chosen to reveal the near-wall structures. For visualization purpose, the y and z axes are equally stretched with a ratio to the x axis of 10. The same length unit is used for these three axes and Reynolds numbers are only marked for discussion purpose. Thus the structures are closer to the wall and more elongated in the streamwise direction than they appear in the plot. In the finite-span case shown in Fig. 16(a), a sheet of vorticity is generated by the wall shear and rolls up into three rows of hairpin-like vortices across the span at about $Re_x = 1.5 \times 10^6$. The vortices are then slightly lifted away from the wall at about $Re_x = 2.0 \times 10^6$. Correspondingly, the vortices are stretched in the streamwise direction in the wall region, resulting in the intensification of streamwise

vorticity as previously shown in Fig. 15(a). The vortices become weaker as the flow relaxes further downstream. As shown in Fig. 16(b), hairpin-like structures are also observed for the full-span case, but they develop in an asymmetric fashion. Similar to the full-span case, vortex stretching in the lifting process induces strong streamwise vorticity in the wall region.

The hairpin structures are better displayed by lowering the iso-levels to $|\omega| = 25$ as shown in Fig. 17. The hairpin-like vortices are initiated across the span at about $Re_x = 2.0 \times 10^6$.

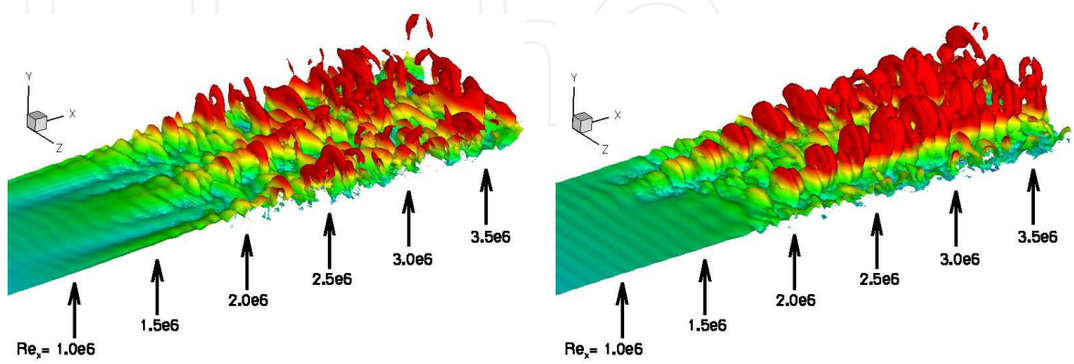

(a) finite span (b) full span

Fig. 17. Iso-surface of instantaneous vorticity magnitude at $|\omega| = 25$, $x : y = 1 : 10$, $x : z = 1 : 10$ (cases 2 and 3)

The legs of the hairpin constitute a pair of counter-rotating vortices oriented in the streamwise direction in the wall region. They are mainly comprised of ω_x and can be difficult to discern in the total vorticity iso-surface plot since the spanwise vorticity ω_z is dominant in the boundary layer. On the other hand, the heads, mainly comprised of ω_z, can be easily identified in the total vorticity variable because they penetrate into the boundary layer about 2.24δ and 2.35δ at $Re_x = 2.5 \times 10^6$ and 3.5×10^5, respectively, where δ is the local unperturbed laminar boundary layer thickness. It is also observed that for the full-span case, the hairpin vortices are tilted higher in the boundary layer than in the finite-span case. The fact that hairpin vortices appear in the full-span case confirms that the initial counter-rotating streamwise vortices are not a necessity in generating the hairpin vortices.

The vorticity concentration can be viewed through vorticity deviation from the basic state as shown in Fig. 18. Looking downstream, close examination reveals that the right leg rotates with positive ω_x and the head with negative ω_z. Three hairpin vortices are annotated on the plot. The legs can be more clearly seen in the iso-surface of ω_x difference in Fig. 19 and the head in the iso-surface of ω_z difference in Fig. 20. Since the value of ω changes, the structures appear to be broken, but other values confirm the coherence of the structures. The hairpin vortices are aligned in the streamwise direction, forming a pattern similar to K-type breakdown, which results from fundamental modes (Klebanoff et al., 1962). In addition, they appear to be highly asymmetric for both cases. Robinson (Robinson, 1991) pointed out that in a turbulent boundary layer, the symmetry of vortex was predominantly distorted, yielding structures designated "one-legged hairpins". Fig. 21 shows a hairpin vortex schematically. Low-momentum fluid is lifted away from the wall between the legs while high-momentum fluid from the freestream is brought down to the wall outside the legs.

The above described motion of the hairpin vortices alters the velocity distribution in the wall region. In the finite-span case, the passage of the counter-rotating vortices generates

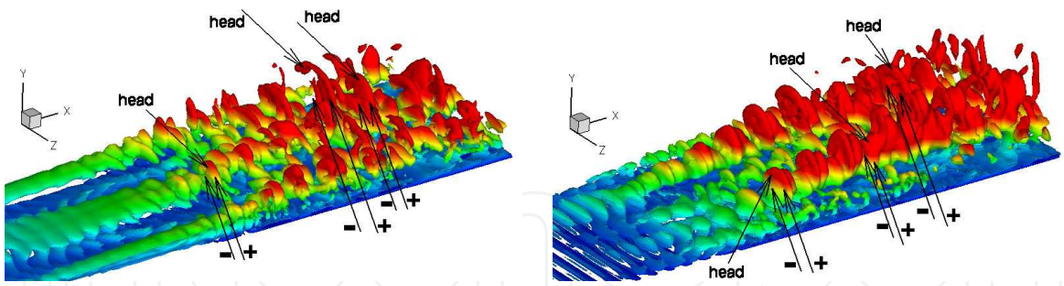

(a) finite span (b) full span

Fig. 18. Iso-surface of instantaneous vorticity magnitude difference at $|\omega| - (|\omega|)_b = 25$, $x : y = 1 : 10$, $x : z = 1 : 10$ (cases 2 and 3)

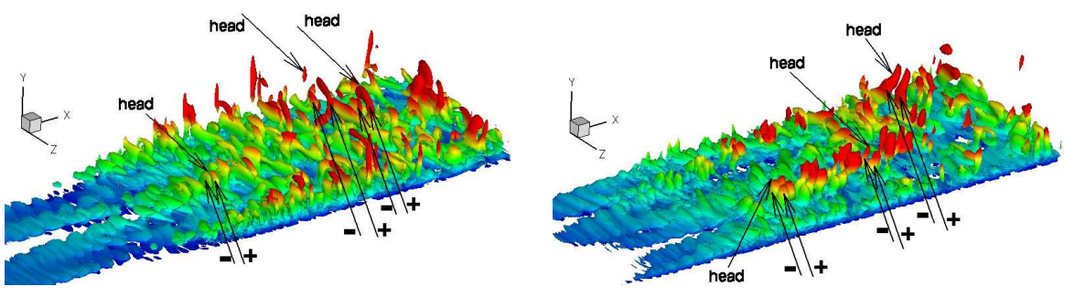

(a) finite span (b) full span

Fig. 19. Iso-surface of instantaneous streamwise vorticity difference at $\omega_x - (\omega_x)_b = \pm 15$, $x : y = 1 : 10$, $x : z = 1 : 10$ (cases 2 and 3)

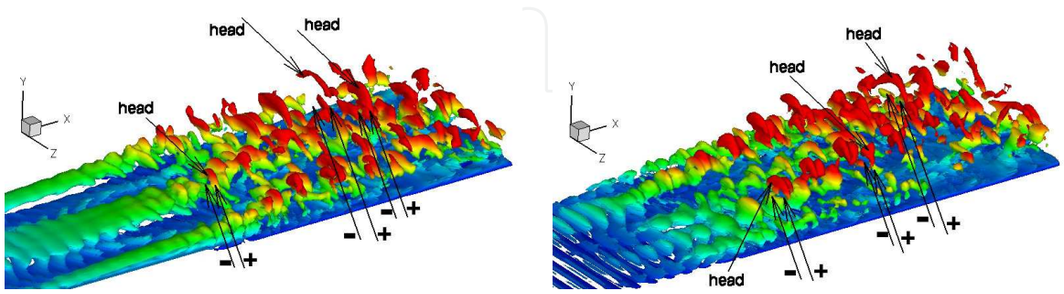

(a) finite span (b) full span

Fig. 20. Iso-surface of instantaneous spanwise vorticity difference $\omega_z - (\omega_z)_b = 25$, $x : y = 1 : 10$, $x : z = 1 : 10$ (cases 2 and 3)

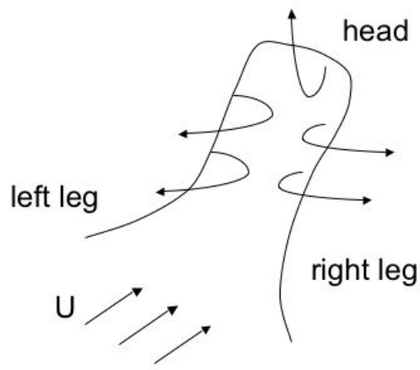

Fig. 21. Schematic of hairpin vortex in pulsed heating

several streamwise streaks in the center region and a low-speed streak is flanked alternately by high and low-speed streaks as shown in Fig. 22(a), which plots the instantaneous streamwise

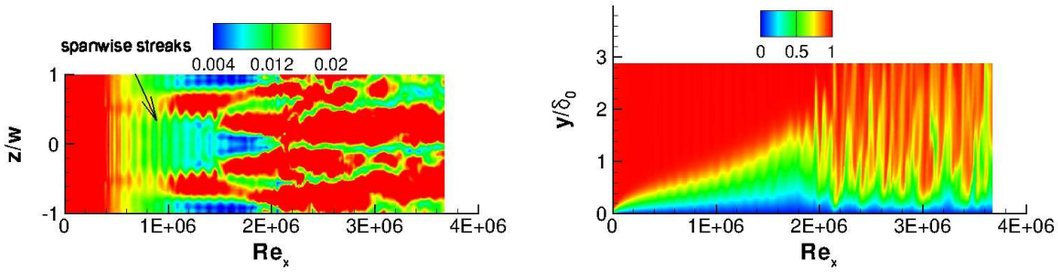

(a) at $y = \delta_0/200$ (b) on the center plane

Fig. 22. Instantaneous u contours for the finite-span case (case 2)

velocity (u) contours at the first grid point above the wall (*i.e.* $y = \delta_0/200$). The central low-speed region is intensified and concentrated towards the center between $1.5 \times 10^6 < Re_x < 2.0 \times 10^6$, resulting in a strong growth of the boundary layer as shown in Fig. 22(b), which depicts the velocity contours on the symmetry plane passing through the center of the domain. At $Re_x = 2.0 \times 10^6$ which is just downstream of the second neutral point, the flow pattern changes dramatically. The low-speed streaks weaken in the wall region and the near-wall low-momentum region becomes thinner as the hairpin vortices pump the low-momentum fluid away from the wall. Strong three-dimensional fluctuations are observed in the upper portion of the boundary layer where the hairpin vortices interact with the high-momentum fluid, leading to the boundary layer distortion.

In the full-span case, the initial spanwise structures are almost two-dimensional in nature. Subsequently, the low-speed streaks are formed at about the location where the hairpin vortices start to appear as shown in Fig. 23(a). This indicates that the low-speed streaks are the footprints of the hairpin vortices. The boundary layer growth is not as strong as that in the finite-span case between $1.5 \times 10^6 < Re_x < 2.0 \times 10^6$ (compare Figs. 23(b) and 22(b)). However, downstream of $Re_x = 2.0 \times 10^6$, strong three-dimensional fluctuations are observed, similar to the finite-span case. It suggests that the non-linear disturbance growth becomes dominant and the initial disturbance form becomes less important. This

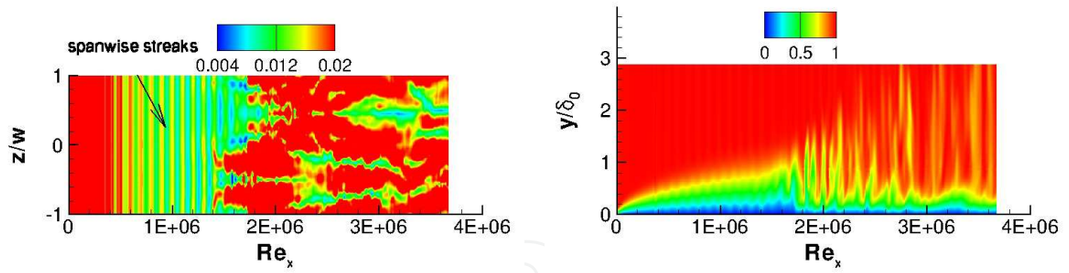

(a) $y = \delta_0/200$ (b) on the center plane

Fig. 23. Instantaneous u contours for the full-span case (case 3)

is confirmed in the disturbance energy growth in Fig. 24, which plots the spanwise-averaged

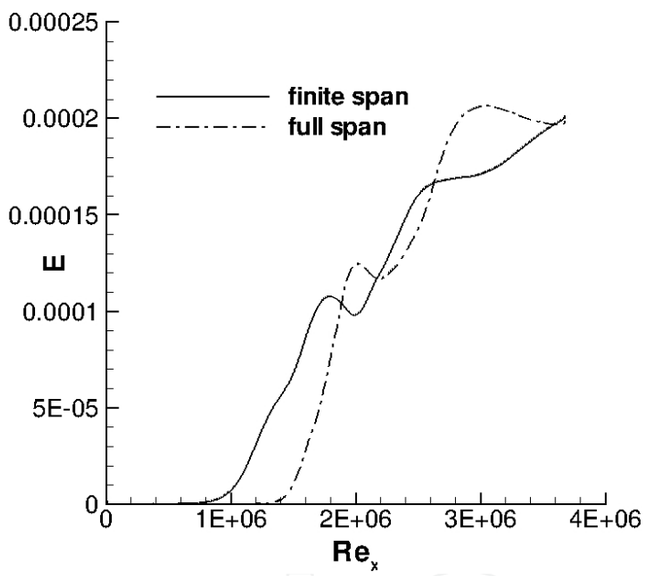

Fig. 24. Spanwise-averaged time-mean total disturbance energy along the x direction (cases 2 and 3)

time-mean total disturbance energy for both finite- and full-span cases. The energy growth in the 2-D perturbations is much weaker than that in the 3-D ones near the bump. However, as the non-linear stability mechanism becomes dominant after about $Re_x = 2.0 \times 10^6$, the disturbance energy growth in both cases becomes comparable.

The accumulated effect of high-frequency pulsing is now described by the time-mean quantities. Only the finite-span results are shown unless otherwise specified. The time-mean pressure ($\bar{p}$) contours are shown on the center plane in Fig. 25. A series of expansion waves is formed at about $Re_x = 2.0 \times 10^6$ and propagates outside the boundary layer. This is caused by the strong boundary layer distortion as shown in the time-mean streamwse velocity contours on the center plane in Fig. 26. The momentum thickness at $Re_x = 2.0 \times 10^6$ is increased by a factor of 1.7 compared to that in laminar flow, indicating that the boundary layer is highly energized downstream of $Re_x = 2.0 \times 10^6$ and shows signs of transition to turbulence. The

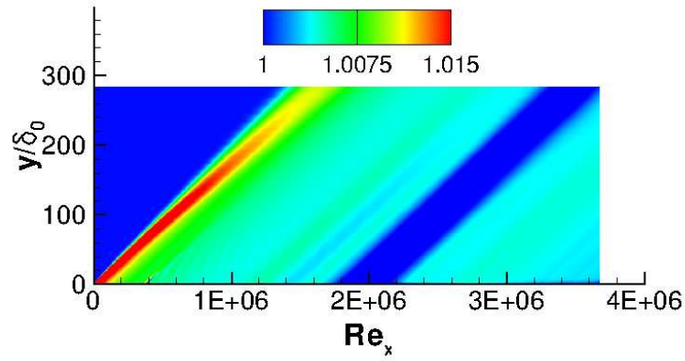

Fig. 25. $\bar{p}$ contours on the center plane for the finite-span case (case 2)

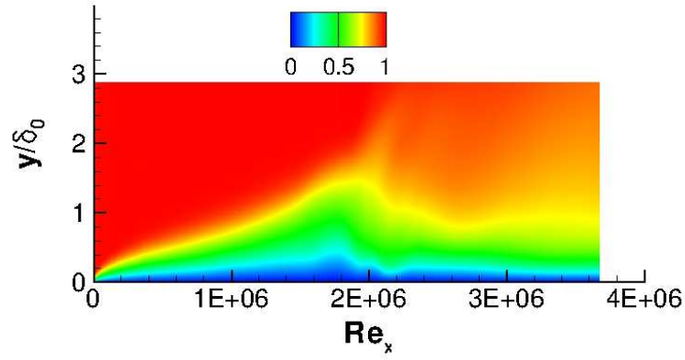

Fig. 26. $\bar{u}$ contours on the center plane for the finite-span case (case 2)

expansion waves in the downstream location are also partially observed in case 1, in which the outlet boundary is set at $Re_L = 1.80 \times 10^6$.

The boundary layer distortion can be assessed by the variation of shape factor H obtained from the mean velocity profile as shown in Fig. 27. The shape factor for the basic state, shown for comparison, reaches an asymptotic value of 2.6 as the flow becomes fully-developed laminar (Fig. 27(a)). With heating, the mean flow is strongly distorted, causing the shape factor to oscillate taking values of 2.85 and 1.35 between $Re_x = 1.5 \times 10^6$ and 2.0×10^6, respectively as shown in Fig. 27(a). A lower shape factor indicates a fuller velocity profile. After $Re_x = 2.0 \times 10^6$ the shape factor decreases rapidly, indicating an increase of the flow momentum in the boundary layer, and starts to level off around $Re_x = 3.0 \times 10^6$. Strong spanwise non-uniformity is observed at $Re_x = 1.5 \times 10^6$ and 2.0×10^6 as shown in Fig. 27(b), while in later stages, only mild distortion is observed and the shape factor reduces to around 1.5, which is close to the turbulent value.

Features of the turbulence statistics are examined through the transformed velocity and Reynolds stresses. Fig. 28 shows the transformed velocity profiles at different downstream locations along the center line (z=0) and the side line of the bump (z=-0.5w). In the viscous sublayer of a compressible turbulent boundary layer where $y^+ < 5$, the turbulent stresses are negligible compared to viscous stress and the velocity near the wall grows linearly with the distance from the wall as $u^+ = y^+$, where u^+ is defined as u_{vd}/u_τ, and y^+ as yu_τ/ν_w. The friction velocity u_τ is defined as $\sqrt{\tau_w/\rho_w}$, where τ_w is wall stress. The detailed formulation of the transformed velocity u_{vd} may be found in Smits and Dussauge (Smits & Dussauge, 2006).

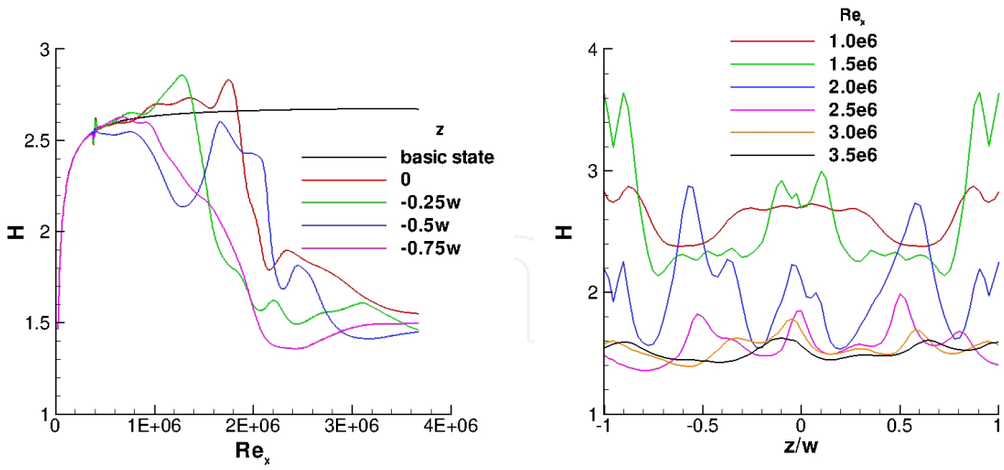

(a) in x direction (b) in z direction

Fig. 27. Shape factor for the finite-span case (case 2)

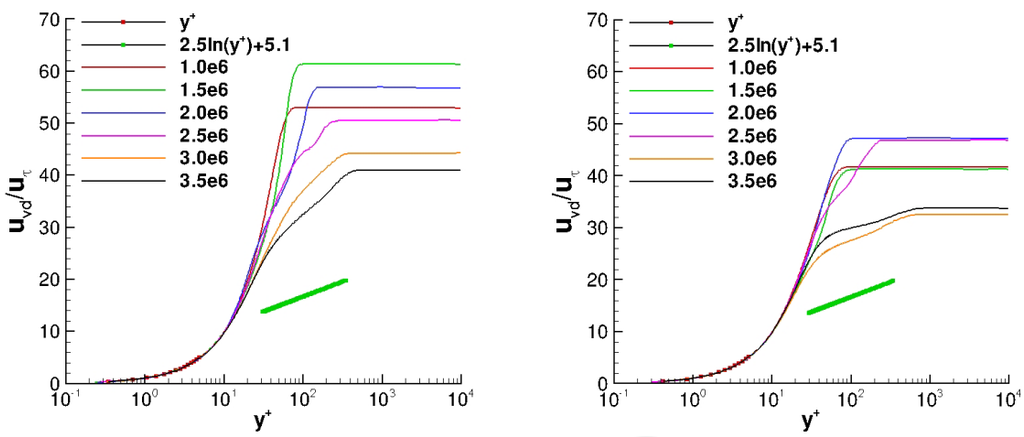

(a) at $z = 0$ (b) at $z = -0.5w$

Fig. 28. Transformed velocity for the finite-span case at different Reynolds number (case 2)

Good agreement is found with the theory at different Reynolds numbers at both center and side locations. The turbulent stresses become large between $y^+ > 30$ and $y/\delta \ll 1$ where the log law holds with $u^+ = \frac{1}{\kappa}\ln(y^+) + C$ with $\kappa = 0.4$ and $C = 5.1$ (Smits & Dussauge, 2006). It is shown in Fig. 28 that the logarithmic region gradually forms with increasing Reynolds number and the velocity slope approaches the log law. However, a large discrepancy remains between the velocity profile at the end of the plate ($Re_x = 3.5 \times 10^6$) and the log law, indicating that the perturbed flow has not reached fully-developed turbulence.

The Reynolds stress profiles are shown to further examine the evolution of the flow. Fig. 29 shows the streamwise Reynolds stress ($\bar{\rho}\overline{u'u'}$) and Reynolds shear stress ($\bar{\rho}\overline{u'v'}$) normalized by the local wall stress (τ_w) at $Re_x = 3.5 \times 10^6$. Note that the local boundary layer thickness δ varies across the span. Experimental and numerical results by other researchers (Johnson

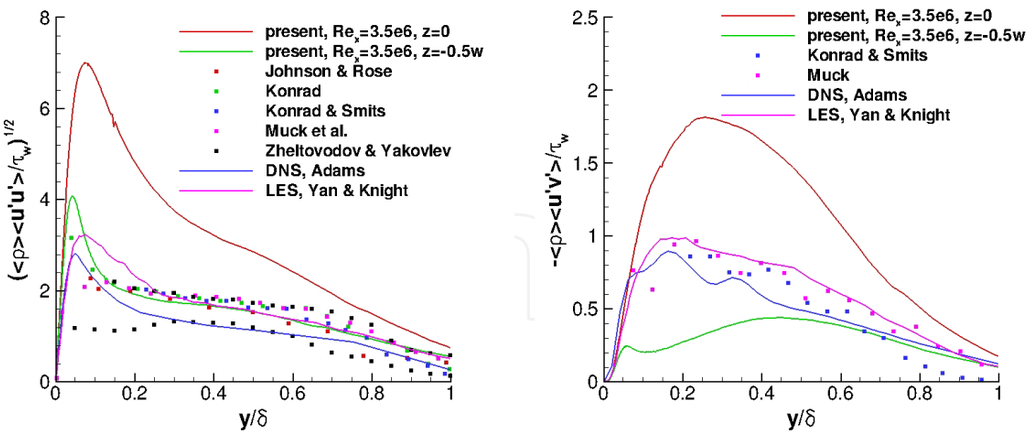

(a) Streamwise stress (b) Shear stress

Fig. 29. Reynolds stress for the finite-span case (case 2)

& Rose, 1975; Konrad, 1993; Konrad & Smits, 1998; Muck et al., 1984; Yan et al., 2002; Zheltovodov et al., 1990) are plotted for comparison. The predicted streamwise Reynolds stress presents a similar trend to the experiments and other numerical data. It reaches the peak at about $y = 0.05\delta$–0.1δ and decays rapidly between $0.1\delta < y < 0.3\delta$. A large spanwise variation of the peak value is observed with the value at $z = 0$ being 1.8 times that at $z = -0.5w$. The same observation holds for the Reynolds shear stress as shown in Fig. 29(b), which is a main source of turbulence production in the wall-bounded flows. The largely scattered data implies that the flow is still in transitional stage, where the strong non-linear disturbances continue to extract energy from the mean flow to maintain their mobility before the energy redistribution equilibrates and the flow exhibits some features of fully-developed turbulence. This is also consistent with that the mean velocity profile being located above the log law in Fig. 28.

Overall, the effect of the disturbance introduced by thermal bumps is observed to follow classical stability theory in the linear growth region. For the parameters considered, the gross features of transitional flow appear near the second neutral point. These features consist of hairpin vortex structures which are non-staggered and resemble K-type transition. Comparison of 3-D (finite span) with 2-D (full span) perturbations effects indicate that although the near field consequences of the bump are profoundly different, the development further downstream is relatively similar, suggesting a common non-linear mechanism associated with the interaction of the disturbance with the boundary layer vorticity.

5. Concluding remarks

This chapter explores the stability mechanism of a thermally perturbed Mach 1.5 flat plate boundary layer. With pulsed heating at frequency of 100 kHz immediately upstream of the first neutral point, non-linear dynamic vortex interactions cause disturbances to grow dramatically downstream and the maximum velocity fluctuation reaches about 20% of u_∞. The inflectional velocity profile makes the flow highly susceptible to the secondary instabilities.

The dynamic vortex interaction at later stages of the boundary layer development is studied by extending the flat plate further downstream. Hairpin structures, considered as one kind of the basic structures in turbulence, are observed and serve to increase the momentum in the wall region. The fact that the hairpin vortices are observed in the full-span case suggests that the initial counter-rotating vortices generated by the finite-span bump might not be directly associated with the formation of hairpin structures. The boundary layer is observed to grow noticeably downstream relative to the unperturbed case. The Reynolds stresses and shape factor profiles suggest that the boundary layer is approaching turbulence, but remains transitional at the end of the computational domain. These results suggest that pulsed heating can be used as an effective mechanism to modulate the supersonic laminar-turbulence transition. One effective way to generate pulsed heating is through plasma actuator where Joule heating and electrode heating are effectively assumed as surface heating.

6. References

Adelgren, R., Yan, H., Elliott, G., Knight, D., Beutner, T. & Zheltovodov, A. (2005). Control of edney iv interaction by pulsed laser energy deposition, *AIAA J.* 43(2): 256–269.

Breuer, K. S. & Haritonidis, J. H. (1990). The evolution of a localized disturbance in a laminar boundary layer. part i. weak disturbances, *J. Fluid Mech.* 220: 569–594.

Breuer, K. S. & Landahl, M. T. (1990). The evolution of a localized disturbance in a laminar boundary layer. part i. strong disturbances, *J. Fluid Mech.* 220: 595–621.

Chang, C. L. (2004). Langley stability and transition analysis code (lastrac) version 1.2 user manual, *NASA/TM-2004-213233*.

Enloe, C. L., Mclaughlin, T. E., Vandyken, R. D., Kachner, K. D., Jumper, E. J., C, C. T., Post, M. & Haddad, O. (2004). Mechanisms and responses of a single dielectric barrier plasma actuator: Geometric effects, *AIAA J.* 42: 595–604.

Fischer, P. & Choudhari, M. (2004). Numerical simulation of roughness-induced transient growth in a laminar boundary layer, *AIAA Paper 2004-2539*.

Gaster, M., Grosch, C. E. & Jackson, T. L. (1994). The velocity field created by a shallow bump in a boundary layer, *Phys. Fluids* 6(9): 3079–3085.

Johnson, D. & Rose, W. (1975). Laser velocimeter and hot wire anemometer comparison in a supersonic boundary layer, *AIAA Journal* 13(4): 512–515.

Joslin, R. D. & Grosch, C. E. (1995). Growth characteristics downstream of a shallow bump: Computation and experiment, *Phys. Fluids* 7(12): 3042–3047.

Klebanoff, P. S., Tidstrom, K. D. & Sargent, L. M. (1962). The three-dimensional nature of boundary-layer instability, *J. Fluid Mech.* 12(1): 1–34.

Konrad, W. (1993). Three dimensional supersonic turbulent boundary layer generated by an isentropic compression, *Ph.D dissertation, Princeton University NJ.*

Konrad, W. & Smits, A. (1998). Turbulence measurements in a three-dimensional boundary layer in supersonic flow, *J. Fluid Mech.* 372: 1–23.

Leonov, S., Bityurin, V., Savischenko, N., Yuriev, A. & Gromov, V. (2001). Influence of surface electrical discharge on friction of plate in subsonic and transonic airfoil, *AIAA Paper 2000-0640*.

Muck, K., Spina, E. & Smits, A. (1984). Compilation of turbulence data for an 8 degree compression corner at mach 2.9, *Report MAE-1642, April*.

Rizzetta, D. P. & Visbal, M. R. (2006). Direct numerical simulations of flow past an array of distributed roughness elements, *AIAA Paper 2006-3527*.

Robinson, S. K. (1991). Coherent motions in the turbulent boundary layer, *Ann. Rev. Fluid Mech.* 23: 601–639.

Roe, P. (1981). Approximate riemann solvers, parameter vectors and difference schemes, *J. Computational Physics* 43(2): 357–372.

Roth, J. R., Sherman, D. M. & P, W. S. (2000). Electrohydrodynamic flow control with a glow discharge surface plasma, *AIAA J.* 38(7): 1166–1172.

Samimy, M., Kim, J.-H., Kastner, J., Adamovich, J. & Utkin, Y. (2007). Active control of high-speed and high-reynolds-number jets using plasma actuators, *J. Fluid Mech.* 578: 305–330.

Schmid, P. J. & Henningson, D. S. (2001). *Stability and Transition in Shear Flows*, Springer-Verlag, New York, NY.

Shang, J. S. (2002). Plasma injection for hypersonic blunt body drag reduction, *AIAA J.* 40: 1178–1186.

Shang, J. S., Surzhikov, S. T., Kimmel, R., Gaitonde, D., Menart, J. & Hayes, J. (2005). Mechanisms of plasma actuators for hypersonic flow control, *Progress in Aerospace Sciences.* 41: 642–668.

Smits, A. J. & Dussauge, J.-P. (2006). *Turbulent Shear Layers in Supersonic Flow, second edition*, Springer, New York, PA.

Tumin, A. & Reshotko, E. (2001). Spatial theory of optimal disturbances in boundary layers, *Phys. Fluid* 13(7): 2097–2104.

Tumin, A. & Reshotko, E. (2005). Receptivity of a boundary-layer flow to a three-dimensional hump at finite reynolds numbers, *Phys. Fluid* 17(9): 094101.

Van Leer, B. (1979). Towards the ultimate conservative difference scheme. v. a second order sequel to godunov's method, *J. Computational Physics* 32: 101–136.

White, E. B., Rice, J. M. & Ergin, F. G. (2005). Receptivity of stationary transient disturbances to surface roughness, *Physics of Fluids* 17: 064109.

Worner, A., Rist, U. & Wagner, S. (2003). Humps/steps influence on stability characteristics of two-dimensional laminar boundary layer, *AIAA J.* 41(2): 192–197.

Yan, H. & Gaitonde, D. (2008). Numerical study on effect of a thermal bump in supersonic flow control, *AIAA Paper 2008-3790*.

Yan, H. & Gaitonde, D. (2010). Effect of thermally-induced perturbation in supersonic boundary layer, *Physics of Fluids* 22: 064101.

Yan, H. & Gaitonde, D. (2011). Parametric study of pulsed thermal bumps in supersonic boundary layer, *Shock Waves* 21(5): 411–423.

Yan, H., Gaitonde, D. & Shang, J. (2007). Investigation of localized arc filament plasma actuator in supersonic boundary layer, *AIAA Paper 2007-1234*.

Yan, H., Gaitonde, D. & Shang, J. (2008). The effect of a thermal bump in supersonic flow, *AIAA Paper 2008-1096*.

Yan, H., Knight, D. & Zheltovodov, A. A. (2002). Large eddy simulation of supersonic flat plate boundary layer using miles technique, *J. Fluids Eng.* 124(4): 868–875.

Zaman, K., Samimy, M. & Reeder, M. F. (1994). Control of an axisymmetric jet using vortex generators, *Phys. Fluids* 6(2): 778–793.

Zheltovodov, A. A., Trofimov, V. M., Schülein, E. & Yakovlev, V. N. (1990). An experimental documentation of supersonic turbulent flows in the vicinity of forward- and backward-facing ramps, *Rep No 2030, Institute of Theoretical and Applied Mechanics, USSR Academy of Sciences.*

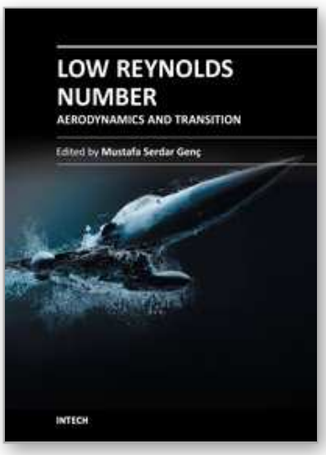

Low Reynolds Number Aerodynamics and Transition

Edited by Dr. Mustafa Serdar Genc

ISBN 978-953-51-0492-6
Hard cover, 162 pages
Publisher InTech
Published online 04, April, 2012
Published in print edition April, 2012

This book reports the latest development and trends in the low Re number aerodynamics, transition from laminar to turbulence, unsteady low Reynolds number flows, experimental studies, numerical transition modelling, control of low Re number flows, and MAV wing aerodynamics. The contributors to each chapter are fluid mechanics and aerodynamics scientists and engineers with strong expertise in their respective fields. As a whole, the studies presented here reveal important new directions toward the realization of applications of MAV and wind turbine blades.

How to reference

In order to correctly reference this scholarly work, feel free to copy and paste the following:

Hong Yan (2012). Thermal Perturbations in Supersonic Transition, Low Reynolds Number Aerodynamics and Transition, Dr. Mustafa Serdar Genc (Ed.), ISBN: 978-953-51-0492-6, InTech, Available from: http://www.intechopen.com/books/low-reynolds-number-aerodynamics-and-transition/thermal-perturbations-in-supersonic-transition

INTECH
open science | open minds

InTech Europe
University Campus STeP Ri
Slavka Krautzeka 83/A
51000 Rijeka, Croatia
Phone: +385 (51) 770 447
Fax: +385 (51) 686 166
www.intechopen.com

InTech China
Unit 405, Office Block, Hotel Equatorial Shanghai
No.65, Yan An Road (West), Shanghai, 200040, China
中国上海市延安西路65号上海国际贵都大饭店办公楼405单元
Phone: +86-21-62489820
Fax: +86-21-62489821

© 2012 The Author(s). Licensee IntechOpen. This is an open access article distributed under the terms of the Creative Commons Attribution 3.0 License, which permits unrestricted use, distribution, and reproduction in any medium, provided the original work is properly cited.

IntechOpen

IntechOpen